Supporting Information

MOCVD-Grown MoS_2 Wafers as a Transfer-Free Platform for Top-Gate Devices via Dry Interface Engineering

Shuhong Li, Juiteng Chang, Keisuke Atsumi, Kosei Matsumoto, Itsuki Tanaka, Tomonori Nishimura, Kaito Kanahashi, Takahiro Nagata, Jun Nara, Yoshiki Sakuma, Emi Kano, Nobuyuki Ikarashi, and Kosuke Nagashio*

E-mail: nagashio@material.t.u-tokyo.ac.jp

MATERIALS AND METHODS

Device fabrication. The top-gate FET structure was prepared directly on monolayer MoS_2/sapphire substrate, as shown in **Figure S1**. For the lithography process, a maskless aligner μMLA (Heidelberg instrument) with double layer resists (PMGI SF5/AZ1500) and NMD-3 developer was used. In the device fabrication flow, the definition of channel geometry is conducted first. The metal mark was deposited at first to define the coordinate among the 15×15 mm^2 substrate, followed by the channel defining enabled by CF_4 etching. It is worth noting that the fluorinated photoresist due to CF_4 etching cannot be removed by lift off process. To achieve successful etching, the double layer resist method was optimized, as the top AZ-1500 was removed in acetone after patterning by photolithography, leaving the bottom PMGI as the mask for CF_4 etching. The typical channel lengths were 10, 15, and 20 μm, while the channel widths were 10 and 20 μm. After the channel definition, the source and drain were patterned, and a 30-nm/1-nm Au/Ni electrode was deposited in an UHV chamber at a base pressure of ~5×10^{-8} Pa with a low deposition rate of 0.0014 Å/s for Ni and 0.15 Å/s for Au. The sample temperature was maintained at 15 °C in the UHV chamber to avoid thermal damage. Then, a 1-nm Er_2O_3 buffer layer was deposited on top of the MoS_2 channel at a partial oxygen pressure (P_{O2}) of 10^{-2} Pa, with the erbium metal heated to 1140 °C at 10^{-5} Pa within a differential-pressure type chamber,[1,2] achieving a deposition rate of approximately 3 pm/s. A 20-nm Al_2O_3 was deposited in a hot wall ALD chamber at 200°C. Subsequently, a 40-nm Au film was deposited as the top gate metal. Alternatively, other gate stacks, ALD-HfO_2/Er_2O_3 buffer layer, ALD-HfO_2/HfO_2 buffer layer, ALD-HfO_2/SiO_2 buffer layer were also tested. The large V_{th} shift without current off-state was basically the same for all the cases.

Characterization. Raman and PL measurements were performed with a Horiba LabRAM HR-800 system equipped with a 488 nm excitation laser. XPS analysis was performed using the PHI Quantes (Ulvac-phi) system. ToF-SIMS measurements were carried out using a ULVAC-PHI TRIFT V nanoTOF instrument. The detailed information can be seen in **Figure S6**. To determine the thickness of Er_2O_3 on alternative SiO_2/Si substrates, GIXR measurements were carried out using Cu Kα radiation at 9 kW with a Rigaku SmartLab. AFM and LFM measurements were conducted with a 0.06 N/m qp-BioAC-3 cantilever (NANOSENSORS) on an Asylum Research Cypher S at room temperature. TDS (ESCO-TDS1200II IR) was performed to detect desorption species from a MoS_2/sapphire wafer annealed under UHV conditions of approximately 4×10^{-8} Pa, using a QMS. The detailed information can be seen in **Figure S8**. TEM images were acquired at an acceleration voltage of 200 kV using a JEM-ARM200F to confirm the quality of the MoS_2/sapphire interface. *I–V* measurements were conducted in a vacuum prober at different temperatures using Keysight B1500.

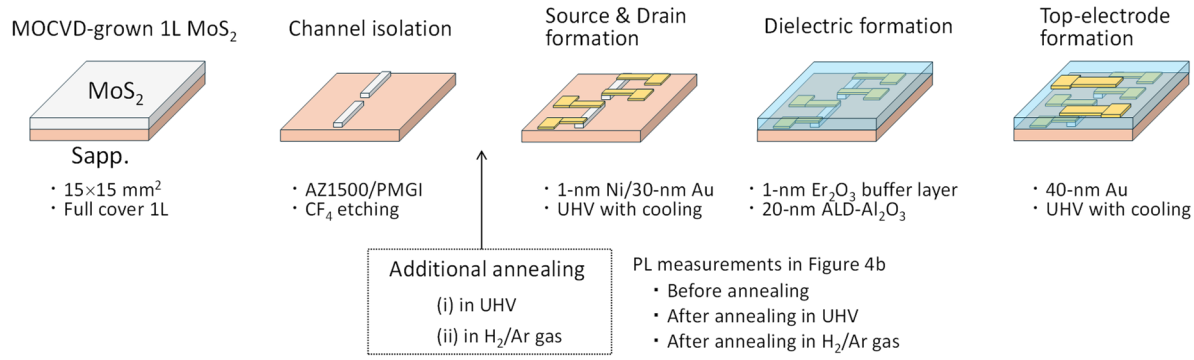

Figure S1. Schematic illustration of the device fabrication process.

Note: For additional annealing, two distinct annealing environments were employed: UHV and H_2/Ar gas ambient. H_2/Ar gas anneal was conducted at different temperature in the RTA system at atmospheric pressure for 30 min at various temperatures. The flow rate of H_2 and Ar were 0.3 L/min and 0.7 L/min, respectively. On the other hand, UHV annealing was conducted in TDS chamber at a base pressure of ~4×10^{-8} Pa. To prevent severe contamination of the TDS chamber, the annealing temperature and duration were limited. The samples were therefore heated to 500 °C or 700 °C and kept at that temp for 15 min in the TDS chamber.

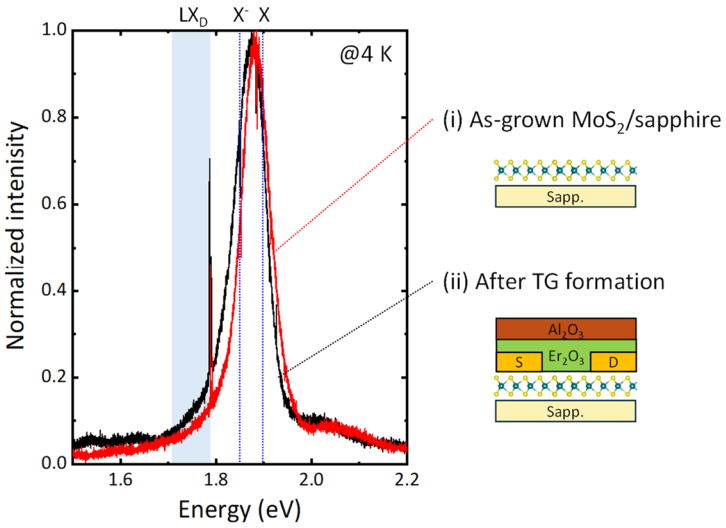

Figure S2. PL spectra of as-grown MoS_2 and MoS_2 with a top-gate insulator. X, X^-, and LX_D are exciton, trion, and defect-related emission, respectively.

Note: In MoS_2, excitons can be trapped at defect states, giving rise to radiative recombination at low temperatures,[3] which is commonly referred to as low-temperature defect-related emission (LX_D). In general, LX_D can be observed in low-temperature PL measurements when the sulfur vacancy density exceeds approximately 10^{12} cm^{-2}. However, when the defect states are filled with electrons, defect-related emission is suppressed;[4] therefore, gate-bias-dependent PL measurements are typically required to clearly identify LX_D. On the other hand, if the defect density is significantly higher than 10^{13} cm^{-2},[5] the defect-related emission becomes stronger than excitonic emission and tends to be less sensitive to the carrier concentration. Considering these factors, although no gate bias was applied in the present low-temperature PL measurements, the absence of LX_D suggests that the defect density in our MoS_2 samples is below 10^{13} cm^{-2}.

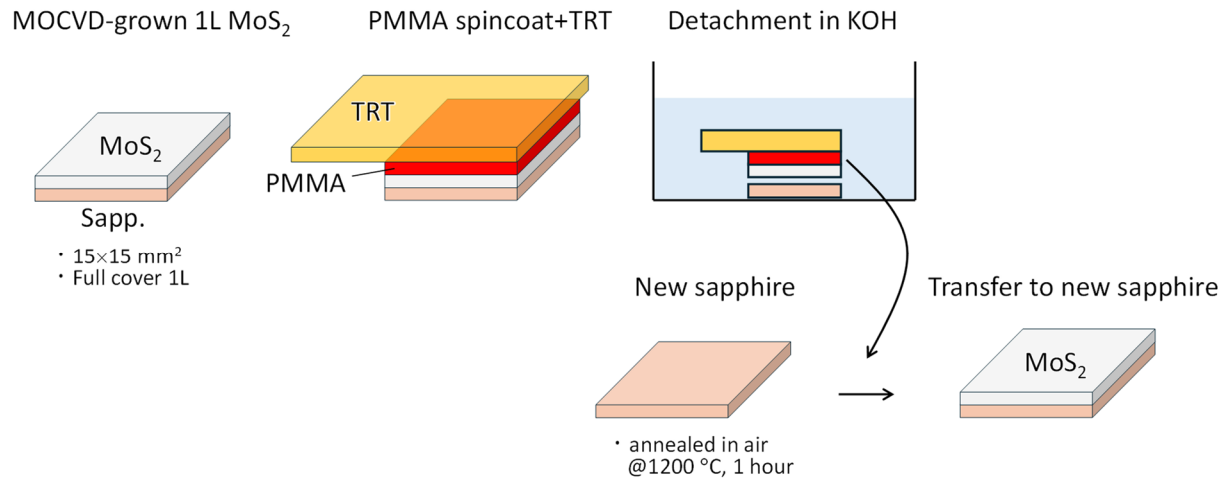

Figure S3. Schematic illustration of the MoS_2 transfer process.

Note: Monolayer MoS_2 grown on sapphire substrates by MOCVD was transferred onto a fresh sapphire substrate using a standard transfer technique. It should be noted that the sapphire substrate was annealed in air at 1200 °C for 1 hour to prepare surface steps aligned along the a-axis $[11\bar{2}0]$. Polymethyl methacrylate (PMMA, MicroChem, 495k) was spin-coated on the MoS_2/sapphire wafer and further supported by thermal release tape (TRT, Nitto, Revalpha). The TRT/PMMA/MoS_2 stack was released from the sapphire wafer in a KOH solution (1 mol/L) and rinsed with deionized water. Following this, the stack was transferred to a fresh sapphire substrate, and the TRT/PMMA film was removed in acetone. For further device fabrication, the same fabrication method described in **MATERIALS AND METHODS** section was applied.

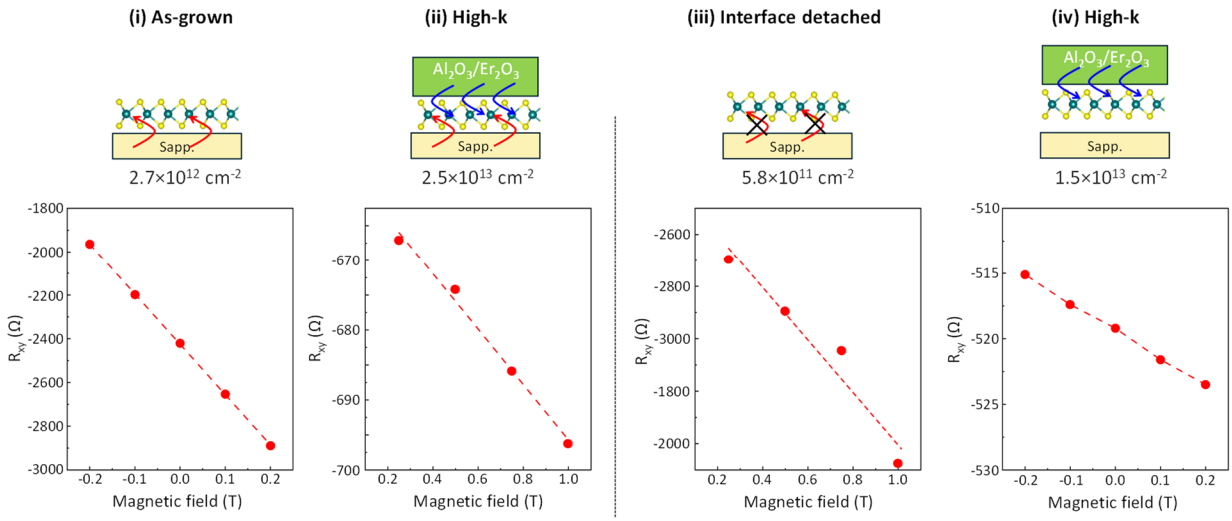

Figure S4. Magnetic field dependence of ΔR_{xy} for different sample conditions under zero gate bias. (i) MoS_2 grown on a sapphire substrate. (ii) MoS_2 grown on a sapphire substrate after deposition of the gate insulator. (iii) MoS_2 transferred onto a fresh sapphire substrate. (iv) MoS_2 transferred on a fresh sapphire substrate after deposition of the gate insulator.

Note: The samples were precisely patterned by CF_4 plasma etching to ensure well-defined device geometry and reliable electrical measurements. In this device configuration, the Hall voltage V_{xy} is given by $V_{xy} = R_h I B + V_{offset}$, where R_h, I, B, and V_{offset} represent the Hall coefficient, excitation current, magnetic field, and offset voltage arising from positional mismatch between Hall probes, respectively. Accordingly, the slope of the magnetic-field dependence of the difference ΔR_{xy} between the off-diagonal resistance $R_{xy} = V_{xy}/I$ and the offset resistance $R_{offset} = V_{offset}/I$ directly yields the Hall coefficient R_h (= $1/qn$), where q is the elementary charge and n is the carrier concentration.

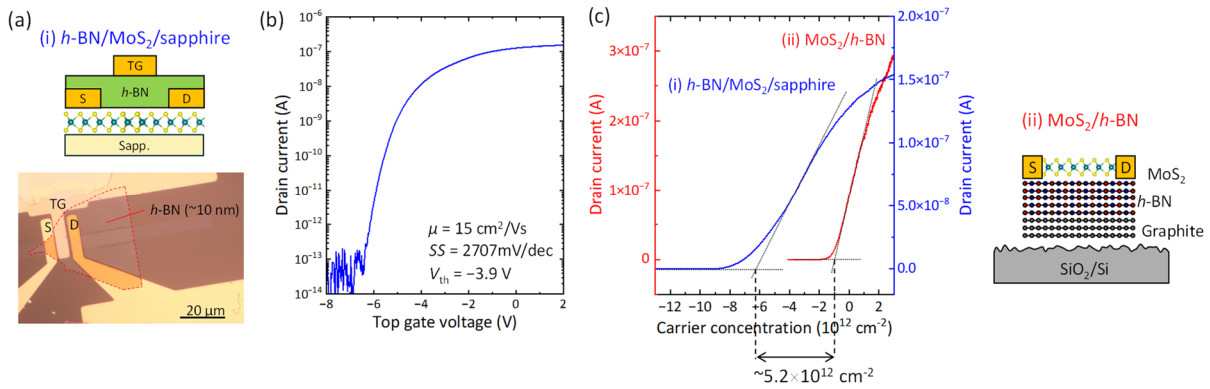

Figure S5. (a) Schematic illustration and optical image of *h*-BN top gate MoS_2 FET. (b) Transfer characteristics of *h*-BN top gate MoS_2 on sapphire substrate. (c) Comparison of charge transfer level between (i) *h*-BN/MoS_2/sapphire and (ii) MoS_2/*h*-BN.

Note: *h*-BN is wildly used to provide an improved electrostatic environment for 2D devices owing to its superior surface flatness and the formation of clean interfaces when employed as a gate insulator. In our previous study of MoS_2 on *h*-BN/graphite back gate,[6] V_{th} was found to be only slightly different from 0 V, serving as a strong indicator of minimal charge transfer at the MoS_2/*h*-BN interface. A similar strategy is adopted here to examine whether the observed charge transfer can be primarily attributed to interactions with the sapphire substrate.

Approximately 10-nm-thick *h*-BN was transferred onto as-grown MoS_2 to serve as the top-gate dielectric. The transfer characteristics measured at room temperature exhibit an on/off current ratio of 10^7, *SS* of 207 mV/dec, and mobility of 15 cm^2/Vs, assuming a dielectric constant $k = 3$ for *h*-BN. Importantly, the extracted V_{th} of −3.9 V indicates that a negative V_{th} shift persists even though the interaction between the top gate insulator and the MoS_2 channel is substantially minimized. The remaining negative V_{th} shift therefore suggests that interactions with the sapphire substrate contribute to electron doping in the MoS_2 channel.

In the present experiment, Hall measurements on the *h*-BN top-gate device were not performed because the available *h*-BN flakes were limited in size, even though relatively large h-BN flakes were obtained, as shown in (a). Instead, we compared the previously reported MoS_2 FETs with an *h*-BN back-gate structure (Fig. 2c in ref. [6]) with the present *h*-BN top-gate MoS_2 FETs fabricated on sapphire substrates, as shown in (c). It should be noted that the transverse axis in (c) was converted from gate voltage to carrier density using the dielectric constant of *h*-BN (ε = ~3) and the *h*-BN thicknesses (both approximately 10 nm). Based on this "rough" estimation, the carrier concentration in the present *h*-BN top-gate device is approximately 5.2×10^{12} cm^{-2} higher than that in the previous *h*-BN back-gate device. This additional carrier density is reasonably attributed to charge transfer from the sapphire substrate to the MoS_2 channel.

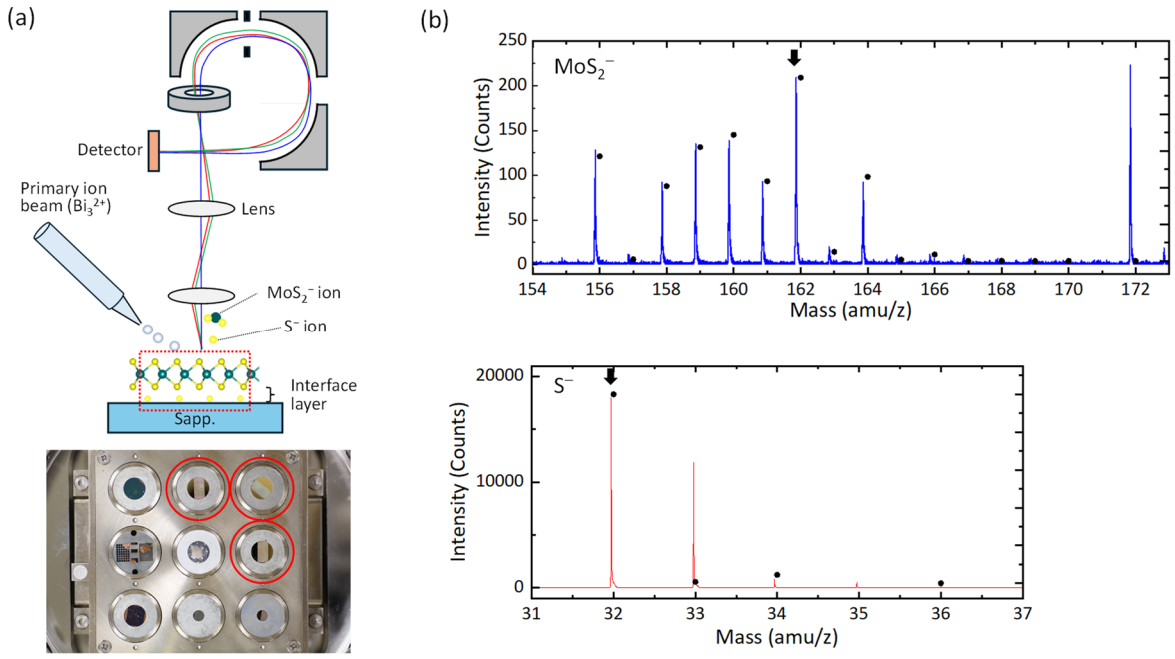

(c)

Mo		MoS_2	
92	0.1477	156	0.13327
94	0.0923	157	0.0021
95	0.1590	158	0.09522
96	0.1668	159	0.14488
97	0.0956	160	0.16052
98	0.2419	161	0.10154
100	0.0967	162	0.23339
		163	0.01159
S		164	0.10719
32	0.9499	165	0.00172
33	0.0075	166	0.0083
34	0.0425	167	6.28233E-5
36	1E-4	168	1.95093E-4
		169	1.46006E-7
O		170	8.24369E-7
16	0.9976	172	9.67E-10
17	0.0004		
18	0.0020		

(d)

Growth temp	900 °C	950 °C	975 °C
MoS_2^- (162) Count	6660	4961	8528
	6246	5099	9199
	6654	5071	8787
S^- (32) Count	224009	121135	227386
	208823	122347	226536
	218140	135693	220314
Average ratio (S^-:MoS_2^-)	33.28	25.06	25.45

Figure S6. (a) Schematic illustration of the ToF-SIMS measurement setup, together with an optical image of the samples inside the analysis chamber. (b) Representative ToF-SIMS spectrum highlighting the S^- and MoS_2^- secondary ion signals. (c) Relative isotope abundances of Mo, S, O, and MoS_2. Red indicates the highest relative abundance. (d) Average S^-:MoS_2^- intensity ratios as a function of temperature.

Note: Although XPS analysis suggests that SO_4^{2-} is specific to the MoS_2/sapphire interface, additional characterization is required because its signal is quite weak. Therefore, time-of-flight secondary ion mass spectrometry (ToF-SIMS)[7,8] was employed owing to its excellent surface sensitivity. **Figure S6a** schematically illustrates the ToF-SIMS principle: primary ion clusters (Bi_3^{2+}) bombard the target surface, generating secondary ions that are separated by their time-of-flight, which is proportional to the square root of the mass-to-charge ratio, enabling elemental and molecular identification. For as-grown MoS_2 on the sapphire substrate, the primary ions can reach the MoS_2/sapphire interface, allowing interfacial analysis. A limitation of ToF-SIMS is its species-dependent detector sensitivity, which prevents quantitative

stoichiometric analysis without reliable standards. Initially, we attempted to analyze the interfacial layer after removing monolayer MoS_2 from the sapphire substrate. However, this approach was unsuccessful due to transfer-induced contamination. Instead, a temperature-dependent analysis was adopted. Thus, changes in the interfacial layer can be indirectly evaluated by examining the S:Mo ratio in samples grown at different temperatures.

In negative-bias mode of ToF-SIMS measurements, S^- exhibits high sensitivity, whereas Mo^- does not. Therefore, MoS_2^- was selected as a proxy for Mo due to its relatively stronger signal. Thus, the S:Mo ratio was extracted from the S^-:MoS_2^- intensity ratio. **Figure S6b** shows a representative ToF-SIMS spectrum highlighting the S^- and MoS_2^- signals. Because both Mo and S possess multiple stable isotopes,[9] the isotopic distribution of MoS_2 was calculated and is shown in **Figure S6c**. The calculated isotopic ratio, plotted as black circles in **Figure S6b**, agrees well with the experimentally measured intensity ratio. The higher experimental intensities observed at m/z = 33 and m/z = 172 suggest the presence of additional species at these mass-to-charge ratios, rather than contributions solely from $^{32}S^-$ and MoS_2^-, respectively. Given that ^{98}Mo and ^{32}S possess the highest natural abundance among their respective isotopes, the $^{32}S^-$ (m/z = 32) and $^{98}Mo^{32}S_2^-$ (m/z = 162) peaks were selected as representative signals. Accordingly, the S^-:MoS_2^- ratio was determined from the intensity ratio of these two peaks. Notably, although $MoSO_2^-$ and MoO_4^- may also contribute to the isotope distribution within the m/z range from 156 to 172 instead of MoS_2^-, detailed peak assignment is not required for determining the S:Mo ratio. **Figure S6d** summarizes the three independent measurements of MoS_2^- and S^- intensities and the averaged S^-:MoS_2^- ratio, which decreases with increasing growth temperature. This trend suggests the presence of a sulfur-related interfacial layer at the MoS_2/sapphire interface and indicates that the formation of interfacial sulfur species is dependent on the growth conditions.

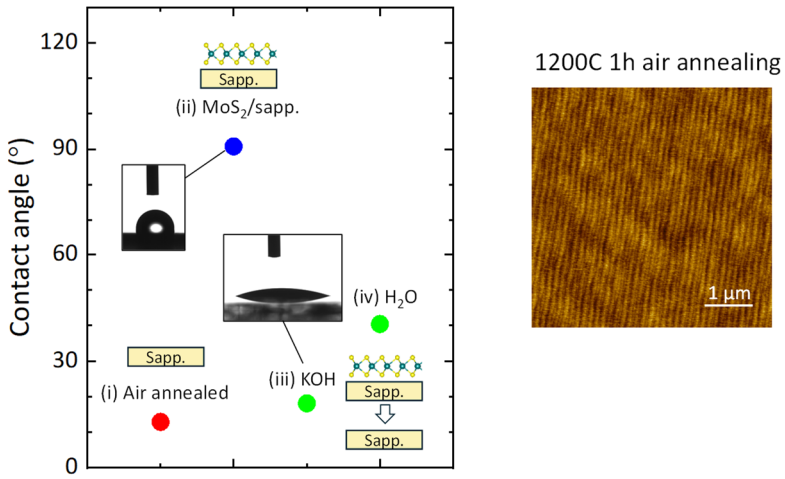

Figure S7. Contact angle measurements for (i) air-annealed sapphire substrate, (ii) As-grown MoS_2 surface on the sapphire substrate, (iii) Sapphire after MoS_2 delamination by KOH solution and (iv) Sapphire after MoS_2 delamination by H_2O.

Note: Based on the present experimental results, an SO_4-related surface termination of the sapphire substrate is expected. Although cross-sectional TEM images are shown in **Figure 4d** of the main text, unambiguous elemental identification, particularly of species terminating the topmost surface of the sapphire substrate, is extremely challenging using TEM. Therefore, characterization techniques with high surface sensitivity are desirable. Here, contact-angle measurements provide a simple yet effective probe of surface termination, as hydrophobic and hydrophilic behaviors are strongly correlated with surface chemical states.[10] (i) After air annealing at 1200 °C, the step and terrace surface was clearly observed, as shown in AFM image. This sapphire substrate exhibits hydrophilic behavior, which can be attributed to the conversion of the high-temperature O-terminated surface into an OH-terminated surface upon exposure to ambient air. (ii) MoS_2 grown on sapphire substrate is hydrophobic due to the dangling bond free surface. (iii) and (iv) It should be noted that MoS_2 delamination was performed using a KOH solution (iii) or H_2O (iv); therefore, sulfate-related species at the MoS_2/sapphire interface may be partially or fully removed during this process. The contact-angle results should thus be regarded as indirect evidence for the interfacial hydrophilicity rather than direct proof of the chemical identity of the interfacial species.

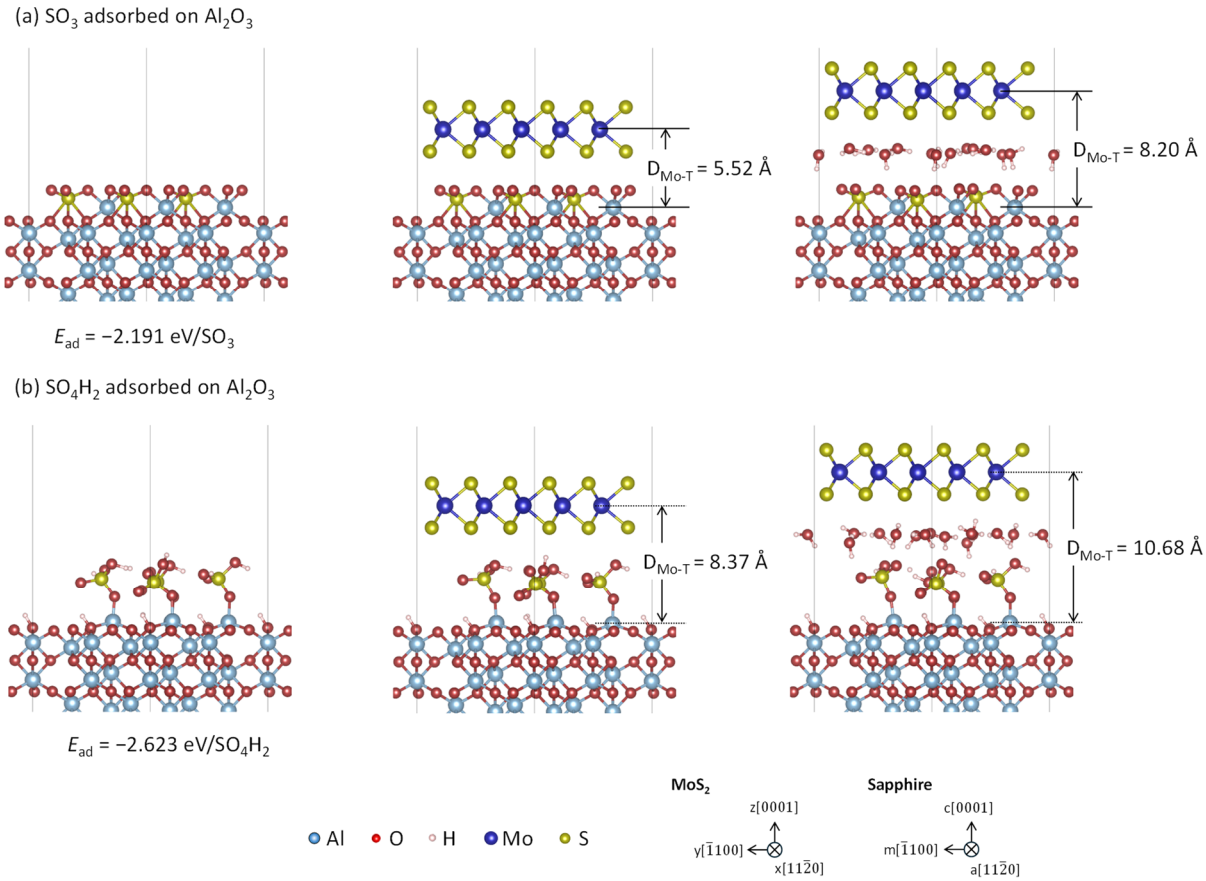

Figure S8 Two conceptual structures simulated by DFT: (a) $4SO_3$ adsorbed on Al_2O_3 and (b) $4SO_4H_2$ adsorbed on Al_2O_3.

Note: Theoretical calculations were performed by using the PHASE/0 code,[11] whose details are available in the previous paper.[12] Adsorption energy (E_{ad}) is defined as $E_{ad} = (E^{molecules/sapphire} - (nE^{molecule} + E^{sapphire}))/n$, where $E^{molecule}$, $E^{sapphire}$, and $E^{molecules/sapphire}$ are the calculated total energies for one molecule, sapphire substrate, and molecules/sapphire, and n is the number of molecules adsorbed on the substrate. Here, the supercell size of sapphire substrate is (2x2) and four molecules are adsorbed on it ($n = 4$). The distance between Mo and the topmost Al atoms (D_{Mo-T}, where T denotes the top Al layer) was calculated using the averaged positions of the surface Al atoms. Both structures (a,b) were hypothetically constructed as representative S^{6+} species suggested by the XPS analysis. Moreover, the concentrations of SO_3 and SO_4H_2 (intuitively expressed as SO_4H_2) were assumed to be identical to the top Al concentration, corresponding to a coverage ratio of 100%. It should be noted that these structures were considered based on ex-situ measurements performed at room temperature after film growth, including XPS and TDS analyses, and are not intended to represent the actual surface structures during growth at temperatures close to 1000 °C. This interpretation is also consistent with the generally accepted understanding that the sapphire surface is predominantly Al-terminated near 1000 °C, whereas it becomes OH-terminated at room temperature.

(a) All the three O atoms in SO_3 are bonded to surface Al atoms, resulting in sixfold Al–O coordination for each surface Al atom, corresponding to an octahedral configuration. In addition, the S atom in SO_3 is bonded to three surface O atoms due to the attractive interaction between the positively charged S atom and negatively charged surface O atoms. Consequently,

the S atom also adopts octahedral-like coordination, appearing to occupy an Al site in sapphire. The SO_3 species exhibit a relatively well-ordered arrangement compared with the SO_4H_2 adsorption case. Furthermore, the surface Al atoms are displaced upward compared with a clean Al_2O_3 surface. We also examined another structure, in which S atom bonds directly to a surface Al atom (not shown), and found it to be less stable than the structure presented here. This instability is attributed to the electrostatic repulsion between the positively charged S and Al atoms.

(b) One O atom in SO_4H_2 is bonded to a surface Al atom, while one H atom dissociates from the molecule and is transferred to a surface O atom. Compared with the SO_3 adsorption case, the SO_4H_2 species exhibit a less ordered arrangement, and the heights of S atoms are not uniform. Although the surface Al atoms are moved upward relative to the clean Al_2O_3 surface, the displacement is smaller than that observed for SO_3 adsorption. We also examined another structure, in which three O atoms in SO_4H_2 are bonded to surface Al atoms, similar to the SO_3 adsorption structure (not shown here), and found it to be less stable than the structure presented here.

Here, we discuss these two structures as possible interfacial models. Previous MOCVD studies have reported pure chalcogen termination for WSe_2,[14,15] MoS_2,[16] and WS_2,[17] and it has also been suggested that Al–O–Se terminations are energetically unfavorable,[14] although the detailed atomic configurations were not discussed. In contrast, the present DFT calculations indicate that sulfur(VI)-related surface configurations, such as SO_3 and SO_4H_2, can be energetically stable. Since surface termination is known to depend strongly on growth conditions,[17] these interface structures should also be considered as plausible candidates consistent with the present XPS results.

Moreover, both models exhibited relatively smooth interfacial morphologies with ordered interfacial water molecules, suggesting that these polar species can coexist without inducing significant structural instability. Moreover, such smooth interfacial morphologies may explain the experimentally observed ~0.3 nm height modulation associated with water molecules (Fig. 2c in the main text). On the other hand, the calculated $D_{Mo–T}$ value for model (b) is larger than that observed for as-grown MoS_2 on the sapphire substrate in the HAADF-STEM images (0.86 nm for the Mo–top Al distance),[12,13] whereas model (a) shows reasonable agreement with the experimental value. Therefore, model (a) may represent one plausible candidate for the interfacial structure. However, since these simulated structures have not yet been experimentally verified, further investigations will be required to clarify the detailed interfacial bonding configuration and spacing. In Fig. 3d, model (a) is adopted for one of plausible candidates.

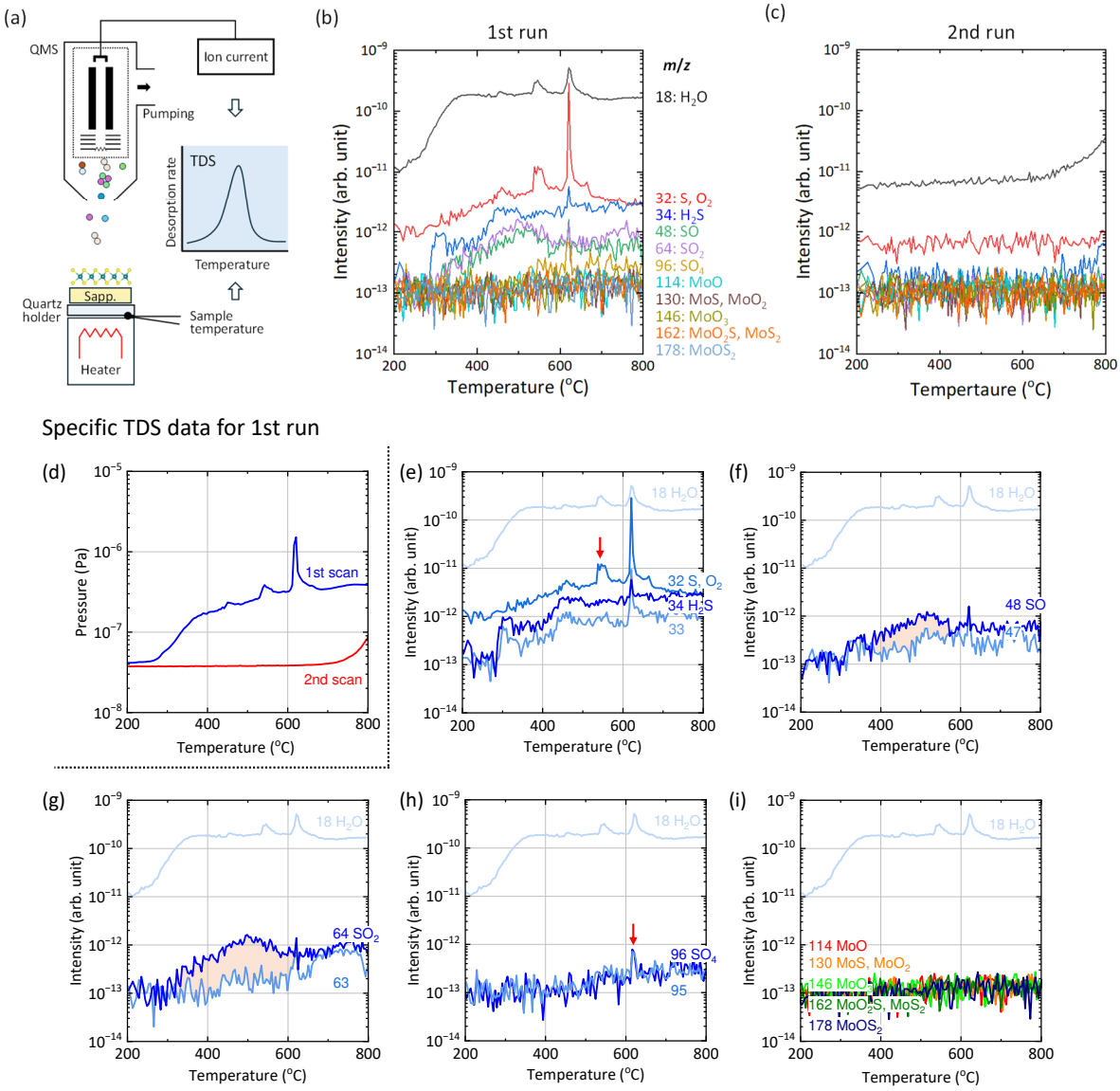

Figure S9. (a) Schematic of the TDS measurement system. (b) 1st TDS run of as-grown MoS_2 on the sapphire substrate. (c) Subsequent 2nd TDS run of the same sample. (d) Total chamber pressure during the 1st and 2nd runs. (e)~(i) TDS spectra of selected S-related species with corresponding background reference channels.

Note: TDS was performed to detect desorption species from a MoS_2/sapphire wafer annealed under UHV conditions of approximately 4×10^{-8} Pa, using QMS.[18–20] The temperature was calibrated using an external thermal couples connected to the Si wafer as standard sample. The ramping rate for sample was set to be 60 °C/min. The growth temperature of MoS_2 sample on sapphire substrate, used for TDS measurements, was 1025 °C.

Quantitative comparison of desorption intensities between different species is generally difficult because the QMS signal strongly depends on ionization cross sections, fragmentation patterns, and mass-dependent transmission efficiency. Moreover, even for the same species, the apparent TDS intensity can be artificially distorted by transient total pressure rises during high-flux desorption events, as shown in **Figure S9d**. Therefore, the TDS spectra obtained in the first and second runs are first compared (**Figure S9b,c**). A pronounced H_2O desorption (m/z = 18) is observed in the first run, accompanied by weaker signals at m/z = 32, 34, 48, 64, and 96,

which may be related to S-containing species. No clear desorption of Mo-related species was detected within our detection limit. To further examine the origin of the S-related signals, the TDS spectra at m/z = 32, 34, 48, 64, and 96 are analyzed in detail in **Figure S9e–i**. For each monitored channel, an adjacent m/z channel, which is not expected to contain the main fragment of the target species, is simultaneously plotted as background reference. This allows us to assess possible artificial variations arising from common-mode effects such as transient pressure increases. Since absolute intensities cannot be directly compared, the analysis focuses primarily on the temperature-dependent spectral shapes.

In **Figure S9e**, the apparent features at m/z = 32 and 34 largely follow the spectral shape of the reference channel at m/z = 33, indicating that common-mode artifacts make a substantial contribution to these signals. However, given their finite intensity, a minor contribution from genuine desorption cannot be entirely excluded. In particular, the small feature observed at ~550 °C (red arrow) at m/z = 32 may reflect the onset of S-related desorption, although this assignment still remains tentative. On the other hand, in **Figures S9f,g**, the signals at m/z = 48 and 64 exhibit deviations from their respective reference channels within the hatched temperature range, indicating possible desorption of S–O–containing species. The m/z = 48 signal can be attributed to SO fragments, while m/z = 64 is consistent with SO_2. In contrast, the peak observed at m/z = 96, indicated by a red arrow in **Figure S9h**, closely resembles the reference-channel behavior, indicating that it is predominantly influenced by pressure-related artifacts and cannot be reliably assigned to a specific desorption species.

Although quantitative evaluation is not feasible from the present TDS data, the above results suggest that SO and SO_2 are the dominant S-containing desorption products during UHV annealing.

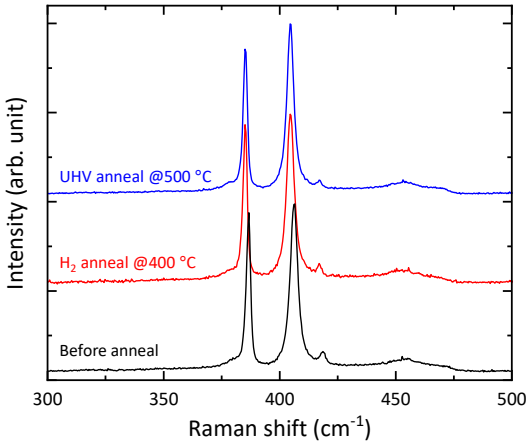

Figure S10. Raman spectra of before anneal, UHV anneal and H_2/Ar anneal.

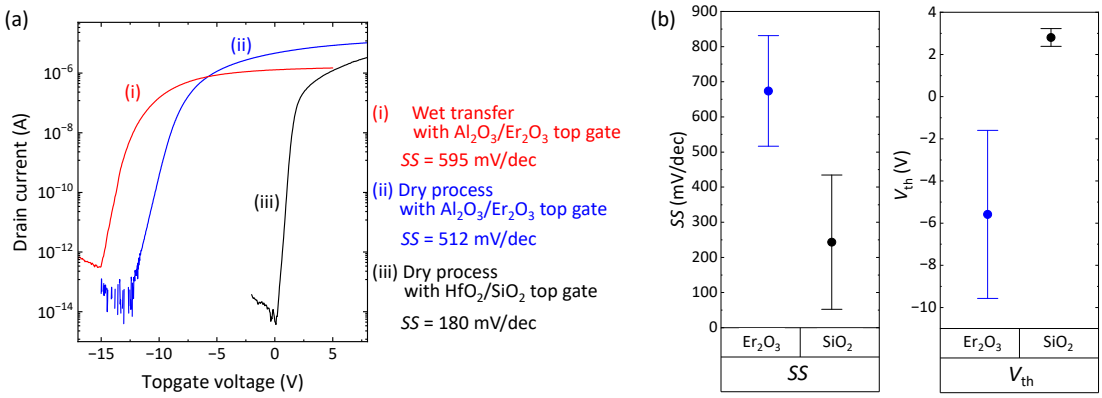

Figure S11. (a) Comparison of transfer characteristics for wet transferred and dry H_2/Ar annealed devices. (b) Comparison of *SS* and V_{th} for two different gate stack devices (Al_2O_3/Er_2O_3 and HfO_2/SiO_2 gate stacks).

Note: (a) The dry H_2/Ar-annealed device exhibits a higher ON current than the wet-transferred device, even though all other process conditions, including the contact formation and top-gate structure, were identical. In terms of V_{th}, the wet-transferred device exhibits a more electron-doped characteristic, which may originate from additional charges introduced during the wet-transfer process. Since a larger amount of charges likely exist on the sapphire surface in the wet-transferred device, the reduced ON-current may be attributed to enhanced carrier scattering induced by these interfacial charges. On the other hand, *SS* values of the dry H_2/Ar-annealed and wet-transferred devices are comparable, suggesting that the interface trap density (D_{it}) is approximately similar for both processes. Based on these results, the improved ON-state performance of the dry H_2/Ar-annealed device is likely associated with a cleaner MoS_2/sapphire interface with reduced charge scattering.

(b) The HfO_2/SiO_2 gate stack exhibits improved device performance compared with the Al_2O_3/Er_2O_3 gate stack, particularly in terms of the reduced variation and enhanced stability of V_{th}. In addition, the average *SS* value is also significantly improved. These results support the effectiveness and reproducibility of the optimized gate-stack design over multiple devices.

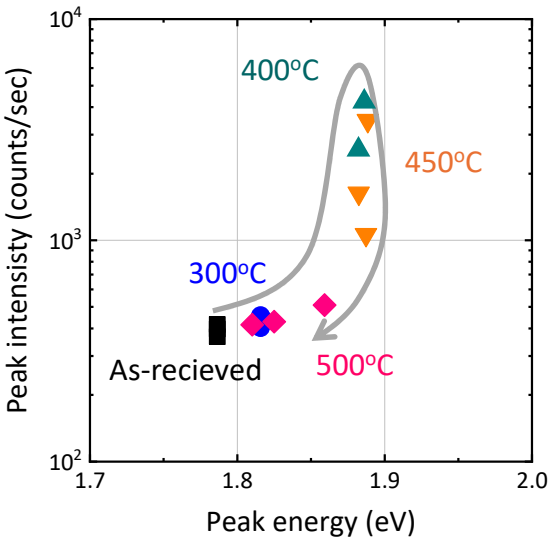

Figure S12. Change of PL intensity after H_2/Ar annealing at different temperatures.

Note: The PL of monolayer MoS_2 was measured at room temperature. The PL peak intensity increased from 300 °C to 400 °C, remained nearly unchanged at 450 °C, and then drastically decreased at 500 °C. These results suggest that the MoS_2 lattice remains largely intact up to 450 °C, while degradation may start to occur at higher temperatures. This observation is consistent with previous reports,[21,22] where MoS_2 decomposition under H_2-containing atmospheres was observed only above ~500 °C. Based on these observations, H_2/Ar annealing can be considered to be effective method to remove sulfate-derived and water-like species at the MoS_2/sapphire interface without degrading MoS_2 channel.

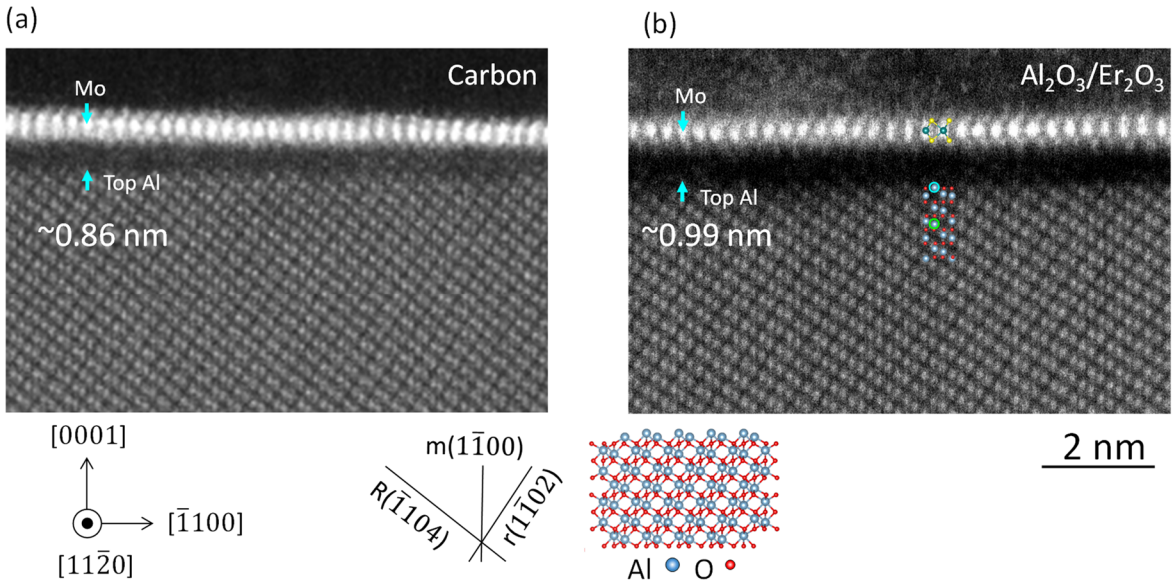

Figure S13. Comparison of HAADF-STEM images of (a) MoS_2 grown on sapphire substrates reported in refs. [12,13] and (b) an Al_2O_3/Er_2O_3 top gate MoS_2 FET fabricated directly on a sapphire substrate. Because dry H_2/Ar annealing was performed during device fabrication, the MoS_2/sapphire interface in (b) appears clearer than that in (a), where amorphous features are observed at the interface. The origin of the relatively long Mo–T distance of 0.99 nm in (b) remains unclear, where T is top Al. The presence of the Al_2O_3/Er_2O_3 top-gate stack, as seen in (b), may contribute to mechanically supporting the MoS_2 film.

References

[1] H. Uchiyama, K. Maruyama, E. Chen, T. Nishimura, K. Nagashio, *Small* **2023**, *19*, 2207394.

[2] S. Li, R. Otake, T. Nishimura, T. Taniguchi, K. Watanabe, Y. Sakuma, K. Nagashio, *ACS Mater. Lett.* **2025**, *7*, 1993.

[3] E. Mitterreiter, B. Schuler, A. Micevic, D. Hernangómez-Pérez, K. Barthelmi, K. A. Cochrane, J. Kiemle, F. Sigger, J. Klein, E. Wong, E. S. Barnard, K. Watanabe, T. Taniguchi, M. Lorke, F. Jahnke, J. J. Finley, A. M. Schwartzberg, D. Y. Qiu, S. Refaely-Abramson, A. W. Holleitner, A. Weber-Bargioni, C. Kastl, *Nat. Commun.* **2021**, *12*, 3822.

[4] Y. Zhu, J. Lim, Z. Zhang, Y. Wang, S. Sarkar, H. Ramsden, Y. Li, H. Yan, D. Phuyal, N. Gauriot, A. Rao, R. L. Z. Hoye, G. Eda, M. Chhowalla, *ACS Nano* **2023**, *17*, 13545.

[5] Y. Zhu, Z. Zhang, Y. Wang, S. Sarkar, Y. Li, H. Yan, L. Ishibe-Veiga, A. Bagri, Z. J. Yang, H. Ramsden, G. Eda, R. L. Z. Hoye, Y. Wang, M. Chhowalla, *Journal of Physical Chemistry C* **2025**, *129*, 8294.

[6] N. Fang, S. Toyoda, T. Taniguchi, K. Watanabe, K. Nagashio, *Adv. Funct. Mater.* **2019**, *29*, 1904465.

[7] J. C. B. D. Vickermann, Ed. , *ToF-SIMS: Materials Analysis by Mass Spectrometry*, IM Publications, West Sussex, **2013**.

[8] I. Tanaka, M. Wei, T. Nishimura, K. Kanahashi, S. Morito, K. Ueno, A. Azizi, K. Nagashio, *Small Methods* **2025**, *9*, e01405.

[9] J. R. de Laeter, J. K. Böhlke, P. De Bièvre, H. Hidaka, H. S. Peiser, K. J. R. Rosman, P. D. P. Taylor, *Pure and Applied Chemistry* **2003**, *75*, 683.

[10] K. Nagashio, T. Yamashita, T. Nishimura, K. Kita, A. Toriumi, *J. Appl. Phys.* **2011**, *110*, 1.

[11] T. Yamasaki, A. Kuroda, T. Kato, J. Nara, J. Koga, T. Uda, K. Minami, and T. Ohno, *Comput. Phys. Commun.* **2019**, *244*, 264.

[12] Y. Sakuma, K. Atsumi, T. Hiroto, J. Nara, A. Ohtake, Y. Ono, T. Matsumoto, Y. Muta, K. Takeda, E. Kano, T. Yasuno, X. Yang, N. Ikarashi, A. Suzuki, M. Ikezawa, S. Li, T. Nishimura, K. Kanahashi, K. Nagashio, *Nat. Commun.* **2026**, *17*, 602.

[13] E. Kano, J. Nara, K. Takenaka, T. Yasuno, K. Atsumi, S. Li, T. Nishimura, K. Kanahashi, J. Uzuhashi, K. Nagashio, Y. Sakuma, N. Ikarashi, *Appl. Phys. Lett.* **2025**, *127*, 252102.

[14] Y. -C. Lin, B. Jariwala, B. M. Bersch, K. Xu, Y. Nie, B. Wang, S. M. Eichfeld, X. Zhang, T. H. Choudhury, Y. Pan, R. Addou, C. M. Smyth, J. Li, K. Zhang, M. A. Haque, S. Fölsch, R. M. Feenstra, R. M. Wallace, K. Cho, S. K. Fullerton-Shirey, J. M. Redwing, J. A. Robinson, *ACS nano* **2018**, *12*, 965.

[15] H. Zhu, N. Nayir, T. H. Choudhury, A. Bansal, B. Huet, K. Zhang, A. A. Puretzky, S. Bachu, K. York, T. V. Mc Knight, N. Trainor, A. Oberoi, K. Wang, S. Das, R. A. Makin, S. M. Durbin, S. Huang, N. Alem, V. H. Crespi, A. C. T. van Duin, J. M. Redwing, *Nature nanotechnol.* **2023**, *18*, 1295.

[16] Y. Xiang, X. Sun, L. Valdman, F. Zhang, T. H. Choudhury, M. Chubarov, J. A. Robinson, J. M. Redwing, M. Terrones, Y. Ma, L. Gao, M. A. Washington, T. M. Lu, G. C. Wang, *2D mater.* **2021**, *8*, 025003.

[17] S. Majumder, N. Shinde, J. Cavin, C. Chen, A. B. Dey, K. V. L. V. Narayanachari, J. Zhang, D. Garcia-Wetten, O. Dieguez, S. Hettler, A. Cohen, D. T. Keane, R. Arenal, J. M. Rondinelli, A. Ismach, M. J. Bedzyk, *ACS appl. nano mater.* **2025**, *8*, 9256.

[18] S. Li, T. Nishimura, M. Maruyama, S. Okada, K. Nagashio, *Nanoscale Adv.* **2022**, *5*, 405.

[19] N. Ikegami, N. Ozawa, Y. Miyakawa, N. H. Norio Hirashita, J. K. Jun Kanamori, *Jpn. J. Appl. Phys.* **1992**, *31*, 2020.

[20] Y.-R. Chang, N. Higashitarumizu, H. Kawamoto, F.-H. Chu, C.-J. Lee, T. Nishimura, R. Xiang, W.-H. Chang, S. Maruyama, K. Nagashio, *Chemistry of Materials* **2021**, *33*, 186.

[21] G. Ye, Y. Gong, J. Lin, B. Li, Y. He, S. T. Pantelides, W. Zhou, R. Vajtai, P. M. Ajayan, *Nano Lett.* **2016**, *16*, 1097.

[22] K. -K. Liu, W. Zhang, Y. -H. Lee, Y. -C. Lin, M. -T. Chang, C. -Y. Su, C. -S. Chang, H. Li, Y. Shi, H. Zhang, C. -S. Lai, L. -J. Li, *Nano Lett.* **2012**, *12*, 1538.